Experimental and numerical studies of intestinal frictions for propulsive force optimisation of a vibro-impact capsule system

**Bingyong Guo · Ellis Ley · Jiyuan Tian ·
Jiajia Zhang · Yang Liu · Shyam Prasad**

© The Author(s) 2020

Abstract This paper studies the intestinal frictions acting on a millimetre-scale self-propelled capsule (26 mm in length and 11 mm in diameter) for small bowel endoscopy by considering different capsule–intestine contact conditions under a wide range of capsule's progression speeds. According to the experimental results, intestinal frictions vary from 7 mN to 4.5 N providing us with a guidance for designing the propelling mechanism of the controllable capsule endoscope. Our calculations show that the proposed vibro-impact mechanism can perform as a force magnifier generating a much larger propulsive force on the capsule than its original driving force. Therefore, the self-propelled capsule is capable of moving in the small intestine under a wide range of friction variation.

B. Guo · E. Ley · J. Tian · J. Zhang · Y. Liu (✉)
College of Engineering, Mathematics, and Physical
Sciences, University of Exeter, Exeter EX4 4QF, UK
e-mail: y.liu2@exeter.ac.uk
B. Guo
e-mail: b.guo@exeter.ac.uk
E. Ley
e-mail: ellis.c.ley@gmail.com
J. Tian
e-mail: jt535@exeter.ac.uk
J. Zhang
e-mail: jz431@exeter.ac.uk

S. Prasad
Royal Devon and Exeter NHS Foundation Trust, Barrack
Road, Exeter EX2 5DW, UK
e-mail: shyamprasad@nhs.net

1 Introduction

Capsule endoscopy [1] has been adopted globally as the gold standard for diagnosing lower gastrointestinal (GI) diseases, such as obscure GI bleeding, the Crohn's disease, the celiac disease, and polyposis syndromes. It equips a miniature camera within a swallowable capsule to screen the lining of the GI tract covering both the small bowel and the colon. The images taken at a few frames per second are transferred to a data receiver, which are examined offline by a gastroenterologist. Compared with the conventional endoscopy, capsule endoscopy provides a new modality which is safe, minimally invasive, sedation-free, patient-friendly, and reliable [2,3]. However, its reliance on peristalsis for passage through the intestine leads to significant limitations [4,5], in particular due to the unpredictable and variable locomotion velocity. Significant abnormalities may be missed, due to intermittent high transit speeds that lead to incomplete visualisation of the intestinal surface. To overcome this limitation, the main challenge is to integrate an active and controllable locomotion mechanism to the current capsule endoscopy, so clinicians can manoeuvre the capsule to the area of interest for a careful examination. In the past decade, several locomotion mechanisms were developed to provide active propulsion for capsule endoscopes, e.g. the

rotating spiral capsule [6], the inchworm-like capsule [7], the legged capsule [8], the paddle-based capsule [9], and the vibro-impact capsule [10]. A detailed survey of these locomotion mechanisms can be found from [11].

The vibro-impact capsule system [10] is self-propelled without any external moving parts, which can be integrated into a standard capsule endoscope, as shown in Fig. 1a. The principle of the vibro-impact self-propulsion is shown in Fig. 1b, where the system consists of a rigid shell M_c, an inner mass M_m connecting to the shell via a helical spring with stiffness k and a damper with damping coefficient c, and a constraint with stiffness k_1 on the shell. The inner mass is excited by a harmonic force F_e, and the impact between the inner mass and the constraint occurs when their relative displacement $X_m - X_c$ is equal to or greater than their original gap G_1. The interaction force between the shell and the inner mass may exceed the intestinal friction F_f leading to a forward or backward motion of the whole capsule.

Inspired by the two-mass system for rectilinear motion [12], the vibro-impact mechanism studied in this work was introduced to the capsule system for motion control by Liu et al. [13]. Comparing with the passive capsule endoscopes, the vibro-impact capsule is active and controllable. Its progression velocity can be controlled by adjusting the frequency and amplitude of the excitation force [14], and a position feedback controller has been designed for such a purpose [15]. Comparing with the other locomotion mechanisms, for example [8,16], the vibro-impact capsule does not have any external moving structure which can reduce the risk of damage to the GI tract. As the vibro-impact capsule is a nonsmooth dynamical system, its dynamics are complex depending significantly on its design parameters and environmental frictions [17]. Therefore, the study of its dynamics under a realistic frictional environment is essential.

According to our preliminary studies [18,19], both numerical simulations and experiments indicate that the system's performance, in terms of progression velocity and energy efficiency, relies on the intestinal friction acting on the capsule. Hence, it is vital to know how much friction will the capsule encounter during its passage through the GI tract. Recent studies on capsule–intestine interaction show that the intestinal friction applying on the capsule ranges from 10 mN to 200 mN depending on capsule's shape, dimension,
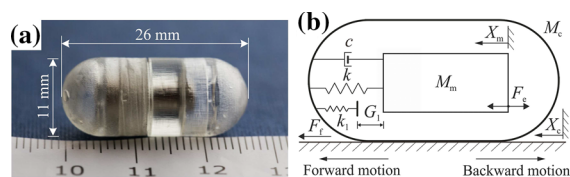

Fig. 1 **a** Photograph of the 3D-printed capsule to be tested in the present work, and **b** the schematic diagram of the self-propelled vibro-impact capsule system

and instantaneous velocity [20–22]. As a consequence, the friction coefficient may vary from 0.08 to 0.2 [20]. To anchor the capsule, capsule surface can be coated with micro-patterned adhesives [16,23] or micro-pillar arrays [24] to increase its friction coefficient up to 0.49. Furthermore, analytical modelling of frictional resistance between a capsule endoscope and the intestine was studied and validated via experiments in [25–27]. However, these studies have not considered different capsule–intestine contact conditions, e.g. partial or full contact with the intestine, since the contact condition may change according to the gesture of the capsule and GI peristalsis. This in turn will affect the intestinal resistance acting on the capsule and further influence the performance and dynamics of the vibro-impact capsule.

Environmental resistant force is generally considered as a negative factor in engineering applications. However, vibration-driven locomotion systems make use of environmental resistant force to achieve rectilinear or planar motions [17,28]. Hence, the dynamics of these systems are affected by the environmental friction significantly, which induces nonlinearity to the system resulting in rich and complex nonlinear phenomena. For example, friction-induced stick–slip motion and multistability were observed in experiments [14,29,30], and sliding bifurcations were studied analytically [28] and geometrically [31]. For the capsule systems, tribological studies always assume that the capsule's motion is uniform, and the environmental friction is constant. Based on our experimental studies [18,19], observations suggest that neither of these assumptions suits well with the vibro-impact capsule system shown in Fig. 1. Therefore, it is crucial to measure the environmental frictions applying on the capsule under various contact conditions and to investigate how these frictions may influence the capsule's dynamics in terms of its average velocity and force amplification. By comparing the measured and theoretical

intestinal frictions and their influences on the capsule's dynamics, experimental and numerical findings in this study can be used as a design guideline to optimise the millimetre-scale vibro-impact capsule prototype [10].

The rest of this paper is organised as follows. Section 2 details the experimental set-up and procedure for four different capsule–intestine contact cases. Mathematical models for friction prediction are studied in Sect. 3, and their comparisons with the experimental results are presented in Sect. 4. Based on the experimental results, Sect. 5 compares the dynamics of the capsule under theoretical and experimental friction models, discusses the force magnification effect of the vibro-impact mechanism, and provides the guideline for design optimisation of a capsule prototype. Finally, conclusions are drawn in Sect. 6.

2 Experimental set-up

This section details the experimental set-up, including the design of a testing rig, four typical capsule–intestine contact cases, and experimental procedure.

2.1 Experimental apparatus

An experimental testing rig was developed to measure the resistant frictional force acting on the millimetre-scale capsule under four various contact conditions and with a wide range of progression speeds for the capsule. The schematic diagram of the testing rig is shown in Fig. 2, and its photograph is presented in Fig. 3. The testing rig consisted of a microcontroller unit, a DC stepper motor, a load cell, and its drive circuit. An Arduino microcontroller Uno Rev3 was used to control a 28BYJ-45 DC stepper motor by sending pulse width modulation (PWM) signal to the drive circuits ULN2003. The DC stepper motor drove the sliding rack at a constant speed through gearing, and the rack pulled the capsule moving inside a synthetic small intestine [32] using a nylon rope. A load cell, YZC-133 100g electronic scale aluminium alloy weighing sensor, consisting of four strain gauges to form a Wheatstone bridge, was mounted at one end of the sliding rack measuring the resistant frictional force acting on the capsule. The Arduino unit recorded the friction force via an AD627 amplifier and connects to a personnel computer (PC) by using a USB cable to achieve bi-

way communication, for which the PC sent commands (CMDs) to control the Arduino unit through a graphic user interface (GUI) in real time, and the Arduino unit sent the measured data to the PC for data logging. The Arduino unit had a six-channel 10-bit on-board analog-to-digital converter which was configured to collect the friction measurement from the load cell at a sampling rate of 50 Hz.

2.2 Experimental set-up and procedure

In this work, four typical capsule–intestine contact cases, as illustrated in Fig. 4, were tested. The experimental set-up for each testing case is given as follows. (i) Case 1: the capsule moved at a constant speed on a flat-open synthetic small intestine supported by a sponge, as shown in Fig. 4a. (ii) Case 2: the capsule moved on a flat-open synthetic small intestine fixed on a solid holder with two circular folds, as presented in Fig. 4b. In order to emulate how the friction force varied when the capsule passes the intestinal fold, two folds were designed in different dimensions of which one was 1.67 mm in height and 3.33 mm in width, while the other one was 2.34 mm in height and 3.09 mm in width, and the smooth section between them was 50 mm. The dimensions of these two folds were chosen within the range of a real porcine small intestine measured in [33]. (iii) Case 3: the capsule moved through a collapsed (loose) synthetic small intestine (25 mm in diameter) fixed to a solid holder with two folds, as shown in Fig. 4c. (iv) Case 4: the capsule moved through a contractive synthetic small intestine whose inner diameter (about 9 mm) was smaller than the external diameter of the capsule (11 mm), as illustrated in Fig. 4d. For each testing case, the experimental procedure is given in Fig. 5.

3 Mathematical modelling of intestinal friction

In Case 1, as shown in Fig. 4a, the capsule moves on a flat-open synthetic small intestine supported by a sponge. As the capsule was pulled at a constant speed in the test, the friction on the capsule is modelled by using the Coulomb friction model, written as

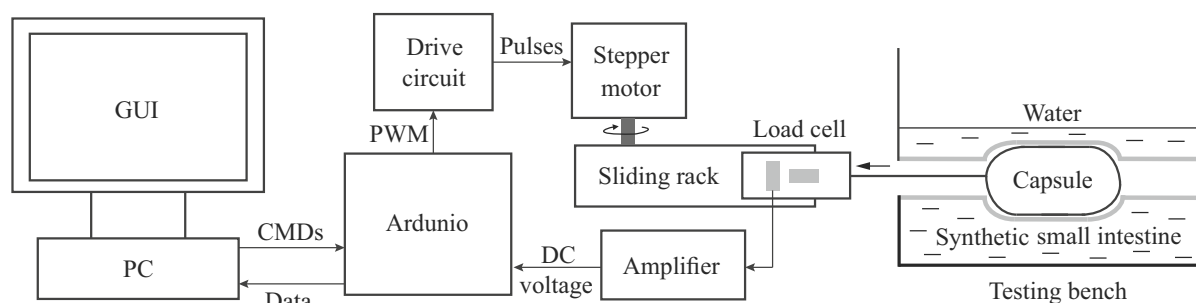$$F_{c1} = F_g = \mu mg, \tag{1}$$

Fig. 2 Schematic diagram of the experimental rig for measuring the frictional resistance acting on the capsule. An Arduino microcontroller unit was used to control a DC stepper motor by sending pulse width modulation (PWM) signals to a drive circuit. The DC stepper motor drove the sliding rack at a constant speed through gearing, and the rack pulled the capsule moving inside a synthetic small intestine using a nylon rope. A load cell was mounted on the sliding rack, and its output was amplified and then collected by the Arduino unit connecting to a personnel computer (PC). The PC sent commands (CMDs) to control the Arduino unit through a graphic user interface (GUI), while receiving the measured data from the Arduino unit for data logging
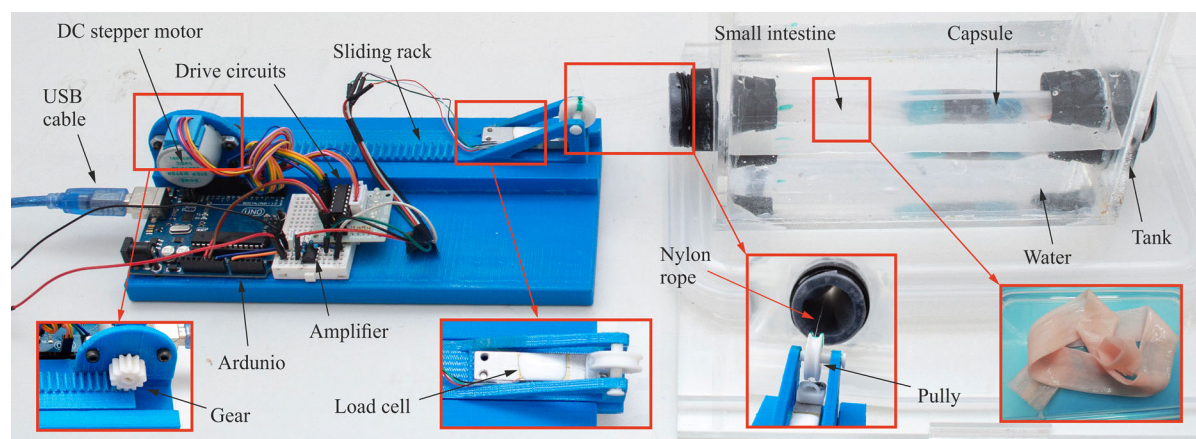

Fig. 3 Photograph of the experimental rig. The capsule moved inside a synthetic small intestine, which was pulled by the sliding rack controlled by a DC stepper motor

where F_g, μ, m, and g represent the friction force due to gravity, friction coefficient between the capsule–intestine contact surface, the total mass of the capsule, and the acceleration due to gravity, respectively.

A finite element (FE) model of the capsule moving on a flat-open small intestine as presented in Fig. 6 was built by using ANSYS WORKBENCH for which material parameter configuration, geometry, contact settings, meshing, constraints, and loads were considered. In the model, the supporting plate, the capsule, and the small intestine were set as the structural steel, the polyethylene, and the viscoelastic material measured in our previous experiments [34], respectively. The dimensions of the capsule and the intestine were set

the same as our experiments, and the contact between the intestine and its supporting base was bonded. Standard gravity was loaded to the capsule, and three mesh layers were set for the intestine in order to provide a fine stress distribution.

For Cases 2 and 3, as shown in Fig. 4b, c, respectively, a general analytical model to predict the friction force between the capsule and the intestine was derived and verified in [33] with the consideration of capsule design parameters, progression speed, tissue mechanical properties, and intestinal circular fold. In the present work, only experimental results will be analysed and used as the design specification for optimising capsule's propulsive force. In addition, the intestine's
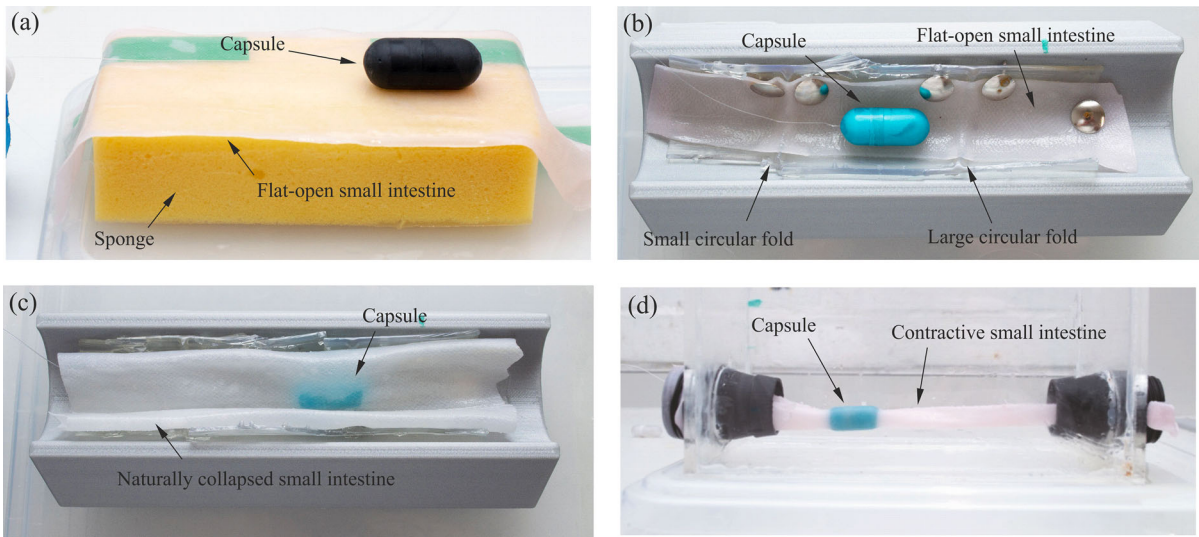
Fig. 4 Four testing cases considering various capsule–intestine contact conditions for which the capsule moves: **a** Case 1: on a flat-open synthetic small intestine supported by a sponge, **b** Case 2: on a flat-open synthetic small intestine fixed to a solid holder with two circular folds, **c** Case 3: in a collapsed (loose) synthetic small intestine (25 mm in diameter) fixed to a solid holder with two circular folds, and **d** Case 4: in a contractive synthetic small intestine whose inner diameter (about 9 mm) is smaller than the capsule's external diameter (11 mm)
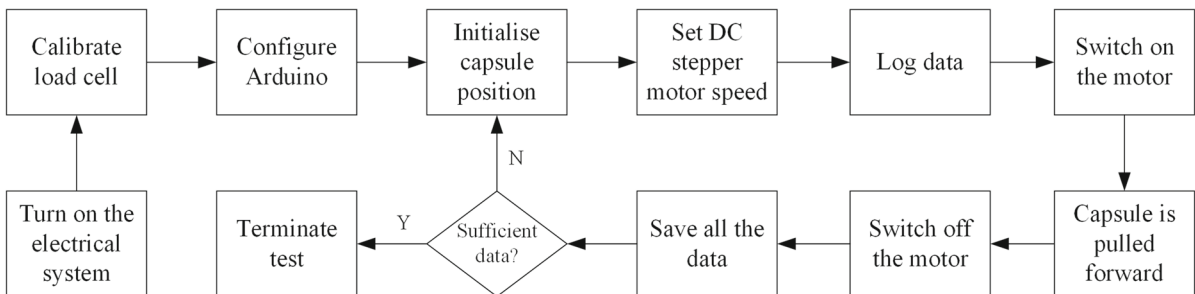

Fig. 5 Flowchart of the experimental procedure

holder consisting of a large and a small circular folds was printed by a stereolithography apparatus 3D printer with an elastic resin, which was much stiffer than the porcine small intestine used in [33]. Therefore, if our optimised propulsive force is greater than the maximal frictional force in the present experimental results, it will be sufficient to drive the capsule in the real scenario.

For Case 4 as presented in Fig. 4d, as the capsule's external radius R_c is larger than the inner diameter of the synthetic small intestine R_i, the capsule is surrounded by the intestine, and viscoelastic deformation of the intestinal wall induces hoop pressure on the capsule. It should be noted that the hoop pressure of the

intestine has been studied in authors' previous paper [34], and the following derivation of the total friction force has referred from the previous work. Under this condition, the friction force acting on the capsule can be written as

$$F_{c4} = F_g + F_h, \tag{2}$$

where F_h represents the friction due to hoop pressure. To model the hoop pressure-induced friction, a local coordinate is defined in Fig. 7a, where x and $R(x)$ represent the axial and radial directions, respectively. As shown in the figure, the capsule is divided into three segments, including a semi-sphere head, a cylindrical
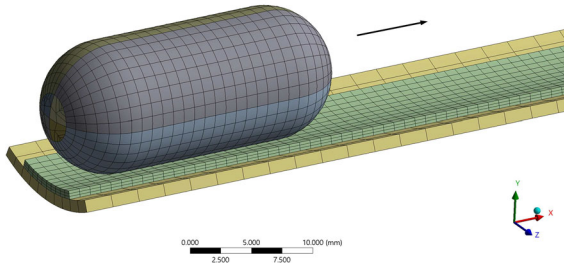
Fig. 6 FE set-up for Case 1: the capsule moves on a flat-open small intestine (green) supported by a workbench (yellow)

body with the length of L, and a semi-sphere tail. In the local coordinate, x_c is the distance from the contact point to the centre of the head in x-axis, and the internal radius of the expanded intestine can be expressed as

$$x_c = \sqrt{R_c^2 - R_i^2} \tag{3}$$

and

$$R(x) = \begin{cases} \sqrt{R_c^2 - (x_c - x)^2}, & x \in [0, x_c]; \\ R_c, & x \in (x_c, x_c + L]; \\ \sqrt{R_c^2 - (x - L - x_c)^2}, & x \in (x_c + L, 2x_c + L]. \end{cases} \tag{4}$$

As the synthetic small intestine is extended by the capsule radially as shown in Fig. 7b, the thickness of the intestinal wall attenuates, and here we assume the sectional area keeps as a constant, given as

$$(R(x) + t_{i,e}(x))^2 - R^2(x) = (R_i + t_i)^2 - R_i^2, \tag{5}$$

where t_i is the original thickness of the intestinal wall. Therefore, the thickness of the attenuated intestinal wall, $t_{i,e}(x)$, can be expressed as

$$t_{i,e}(x) = \sqrt{(R_i + t_i)^2 + R^2(x) - R_i^2} - R(x). \tag{6}$$

So, intestinal hoop strain can be obtained as

$$\epsilon = \frac{R_i - R(x)}{R_i}. \tag{7}$$

In the present work, the Maxwell model [34] was used to describe the viscoelastic property of the synthetic small intestine as illustrated in Fig. 7c for which E_1, E_2, and η_1 represent the Young's moduli of

the springs and the damping coefficient, respectively. Here, the viscoelastic property of the intestine can be expressed using the hoop stress as

$$\tau(x) = \epsilon \left(E_1 e^{-\frac{E_1}{\eta_1} \frac{x}{V_c}} + E_2 \right), \tag{8}$$

where V_c is the constant progression speed of the capsule. The relationship between the hoop pressure and the hoop stress is the same as the pressure vessels [35], which can be given as

$$P_h(x) = \frac{t_{i,e}}{R(x)} \tau(x). \tag{9}$$

For the semi-sphere head section ($0 < x \leq x_c$), the hoop stress acting on the head can be decomposed into two parts: (i) the hoop stress along x-axis contributing to the resistance directly, marked as f_{hr}, and (ii) the hoop stress along $R(x)$ contributing to the resistance based on the Coulomb friction model, marked as f_{hf}, which are given by

$$f_{hr} = \frac{2\pi}{R_c} \int_0^{x_c} (x_c - x) P_h(x) R(x) \sqrt{1 + R'^2(x)} \mathrm{d}x, \tag{10}$$

and

$$f_{hf} = \frac{2\pi \mu}{R_c}$$
$$\int_0^{x_c} \sqrt{R_c^2 - (x_c - x)^2} P_h(x) R(x) \sqrt{1 + R'^2(x)} \mathrm{d}x, \tag{11}$$

where $R'(x)$ is the derivative of $R(x)$ with respect to x.

For the cylindrical body section ($x_c < x \leq x_c + L$), the hoop stress is normal to the capsule surface, and hence, only introduces the Coulomb friction which can be written as

$$f_{bf} = 2\pi \mu \int_{x_c}^{x_c+L} P_h(x) R(x) \sqrt{1 + R'^2(x)} \mathrm{d}x, \tag{12}$$

where $R(x) = R_c$ and $R'(x) = 0$.

For the semi-sphere tail section ($x_c + L < x \leq 2x_c + L$), hoop-induced friction is similar to the counterpart of the head section, including (i) the hoop resistance on
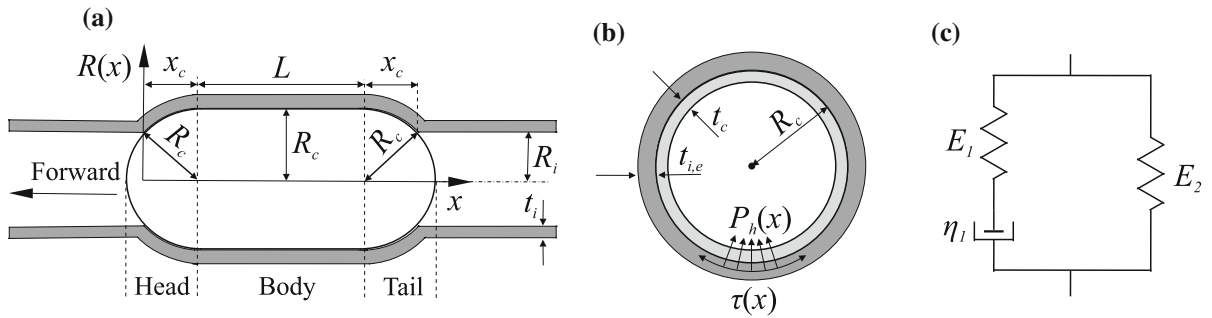
Fig. 7 a Geometric dimension of the capsule surrounded by the small intestine for Case 4 for which the capsule can be divided into three parts: head, body, and tail. **b** Section view of the capsule–intestine interaction perpendicular to the x-axis. **c** Three-element Maxwell model to depict the stress–strain relationship of the small intestine with two springs and one damper. These diagrams were adopted from [34]

the tail f_{tr} and (ii) the hoop stress-induced Coulomb friction on the tail f_{tf}, which can be written as

$$f_{tr} = \frac{2\pi}{R_c} \int_{x_c+L}^{2x_c+L} (x_c - x) P_h(x) R(x) \sqrt{1 + R'^2(x)} \mathrm{d}x, \tag{13}$$

and

$$f_{tf} = \frac{2\pi\mu}{R_c} \int_{x_c+L}^{2x_c+L} \sqrt{R_c^2 - (x_c - x)^2} P_h(x) R(x) \sqrt{1 + R'^2(x)} \mathrm{d}x. \tag{14}$$

Finally, the friction due to hoop pressure can be written as

$$F_h = f_{hr} + f_{hf} + f_{tr} + f_{tr} + f_{tf}, \tag{15}$$

and the total friction force in Eq. (2) can be rewritten as

$$F_{c4} = F_g + F_h = F_g + f_{hr} + f_{hf} + f_{tr} + f_{tr} + f_{tf}. \tag{16}$$

The detailed modelling of the above model has been reported in [36], and the relevant parameters used in the model have been identified experimentally in [34], which are summarised in Table 1. The geometric dimension of a capsule used in the present study was the standard dimension of a market-leading capsule endoscope [37]. As the original diameter of the synthetic small intestine used in this work was about 25 mm [32], in order to test Case 4, the original small intestine was

Table 1 Geometric dimension of the capsule and mechanical properties of the synthetic small intestine

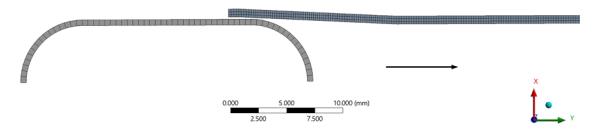| Parameter	Unit	Value
R_c	mm	5.50
t_c	mm	0.50
L	mm	15.00
m	g	3.462
R_i	mm	$4.4 \sim 4.8$
t_i	mm	0.69
E_1	kPa	196.43
E_2	kPa	757.48
η_1	MPa s	5.36
μ	–	0.2293

Fig. 8 FE set-up for Case 4: the capsule moves in a circumferentially contractive intestine

cut and self-assembled. So, its inner radius after self-assembling was not exactly homogenous, varying from 4.4 mm to 4.8 mm. Identification of friction coefficient μ between the capsule and the intestinal surface was carried out by lifting one side of the supporting surface slowly until the stationary capsule started to move, and the friction coefficient was determined by the angle of the surface slope at that moment.
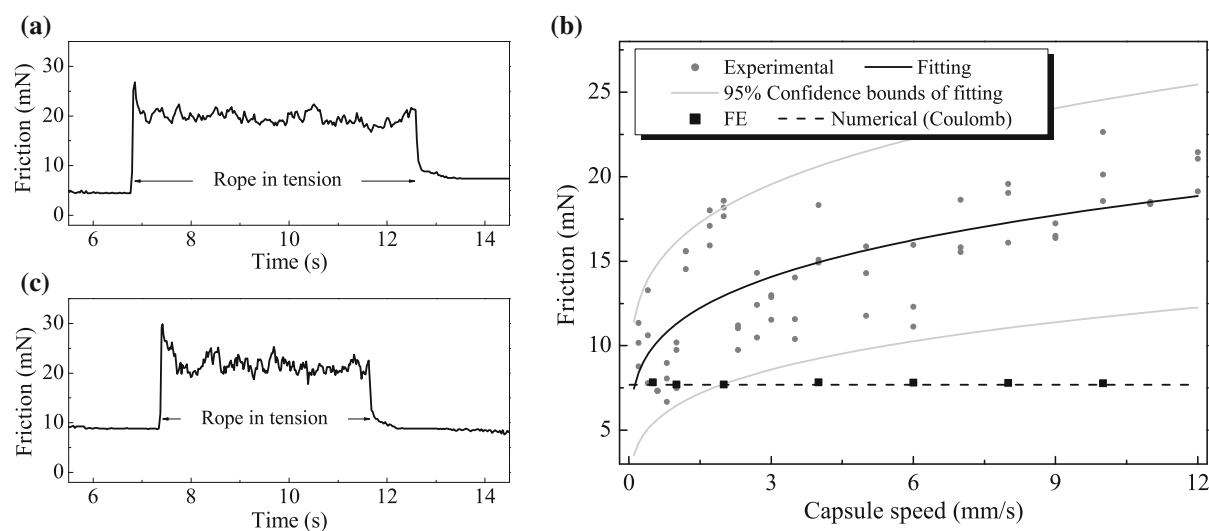
Fig. 9 Experimental time histories of Case 1 for which the capsule was pulled on a flat-open synthetic small intestine at the constant progression speeds of **a** 8 mm/s and **b** 12 mm/s, and **c** average friction as a function of capsule's speed. Black dots represent average frictions, black solid line denotes the fitting of the averaged frictions, its 95% confidence bounds are depicted by grey lines, black squares represent FE results, and black dash line represents the friction prediction by using the Coulomb model (1)

As the computation of the three-dimensional FE model for Case 1 was time-consuming, a two-dimensional axisymmetric model as shown in Fig. 8 was developed for Case 4 in order to improve computing efficiency. In this case, gravity was not applied, and three mesh layers of the intestine were also considered in the model.

4 Experimental and numerical results

In this section, experimental and numerical results are compared, and all the testing cases are discussed. Typical time histories of friction measurement are presented to describe the fluctuation of the intestinal friction, and the averaged frictions are also given for a wide range of capsule's progression speeds.

4.1 Case 1: moving on a flat-open intestine

For Case 1, two typical time histories of measured friction are presented in Fig. 9a, b for which the capsule moved on the flat-open synthetic small intestine at a constant speed of 8 mm/s and 12 mm/s, respectively. Before the DC stepper motor was turned on for pulling the capsule, the measurement was nonzero due to some pretension of the nylon rope when the capsule was moved to an arbitrary initial position. After the motor was turned on, the rope was in tension, and the capsule started to move forward whose friction was increased suddenly. Here, the data when the rope was in tension were used to compute the average friction for this trial. As can be observed from Fig. 9a, b, the average frictions of the capsule were 19.57 mN and 21.45 mN when the capsule was pulled at 8 mm/s and 12 mm/s, respectively.

Extensive experimental tests for a wide range of progression speeds were conducted, and the average friction for each trial is summarised in Fig. 9c, where black dots represent the averaged measurements for the time traces in Fig. 9a, b when the rope was in tension, and black solid line denotes the fitted result of the experimental data. Based on the experimental data, the fitted friction–speed relationship can be written as

$$F_{c1e} = 8.778V_c^{0.25} + 2.518, \tag{17}$$

where V_c is capsule's progression speed. The 95% confidence bounds of the fitting are also presented in Fig. 9c, and it can be seen that all the experimental data are within the 95% confidence bounds. However, the r-squared fitting goodness is about 0.5481, where the value of 1 represents perfect fitting. The main reason is
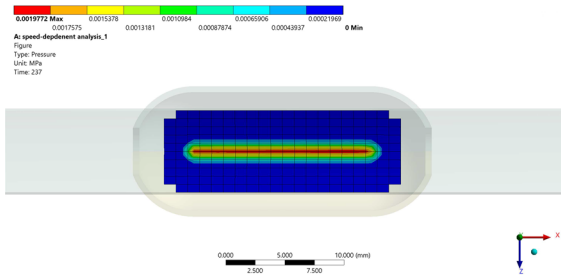
Fig. 10 Bottom view of the pressure distribution for Case 1. The capsule moved at 4 mm/s on the intestine, and the rectangular area enclosed by the blue area is the capsule–intestine contact area

that the measurement noise, about 5 mN according to Fig. 9a, b, is relatively large compared to the averaged frictions in Fig. 9c. In addition, as can be seen from the figure, the frictions obtained by numerical and FE simulations by using the Coulomb model (1) are about 7.8 mN, but cannot give an accurate prediction when the capsule speed is greater than 2 mm/s. Therefore, when the capsule moves on a flat-open intestine, capsule's speed is one of the key factors which influences the intestinal friction on the capsule, and the new fitted model (17) is recommended.

Figure 10 presents the pressure distribution when the capsule moved at 4 mm/s on the small intestine. As can be seen from the figure, the rectangular area enclosed by the blue area which is about 15 mm in length and 2.6 mm in width is the capsule–intestine contact area, and its average contact pressure is about 220 Pa.

4.2 Case 2: moving on a flat-open intestine with two circular folds

In Case 2, a piece of flat-open small intestine was fixed on a 3D-printed arc-shape holder with two bumps to mimic intestinal circular folds, where the small fold was 1.67 mm in height and 3.33 mm in width, and the large fold was 2.34 mm in height and 3.09 mm in width. These dimensions were obtained from Sliker *et al* [33] who scanned the tissue morphology of a porcine intestine by using a laser sensor. A typical time history of the measured friction force is presented in Fig. 11a for which capsule's progression speed was 8 mm/s, and the peak and average frictions are compared in Fig. 11b for different progression speeds. As can be seen from Fig. 11a, capsule's friction is considered for different stages with their illustrations shown in Fig. 11c. It can be seen that the capsule experienced peak frictions at

① and ⑥ when it began to pass over the folds, and its friction dropped off dramatically at ③ and ⑧ due to reduced contacts with the folds. When the capsule moved on the flat intestine as ⑤ and ⑨, its average friction was closed to the average friction measured in Fig. 9c. According to our experimental results, the peak frictions at ① and ⑥ were 37.5 mN and 88.2 mN, respectively, and the average friction at ⑤ was 15.6 mN. Then, these values were used to construct Fig. 11b. Observed from the figure, it reveals that the higher the fold is, the larger the peak friction is, and capsule's peak frictions are much larger than its average frictions varying from 7 mN to 23 mN when the capsule is pulled at the progression speed between 0.7 mm/s and 12 mm/s.

4.3 Case 3: moving in a collapsed intestine with two circular folds

In Case 3, an entire small intestine was used and its inner diameter and thickness were 25 mm and 0.69 mm, respectively. The bottom half of the intestine was fixed onto the arc-shape holder with two bumps, and its top half collapsed naturally on the capsule due to gravity. The contact condition for Case 3 was more complex than Case 2 as part of the small intestine covered the capsule, contributing additional friction to the capsule. A typical time history of the measured friction is presented in Fig. 12a. The trend of friction fluctuation is the same as the time history recorded for Case 2 as shown in Fig. 11a, c, which can also be used to determine the position of the capsule in Case 3. However, due to the natural collapsing of the intestine, peak and average values of the friction are much larger than the ones recorded in Case 2.

In total, 14 tests were carried out for Case 3 based on the experimental set-up shown in Fig. 4c, and peak and average values of the measured friction are presented in Fig. 12b, where black squares, grey dots, and grey triangles represent the peak friction values of the large circular fold, the small circular fold, and the average friction for each test, respectively. Compared with the experimental results for Case 2 as shown in Fig. 11b, the intestinal frictions of this case are greater and more fluctuant due to the nonuniform contacts between the intestine and the capsule. As mentioned in Sect. 2.2, the top half of the intestine contacted with the capsule partially, and it was observed that contact conditions varied
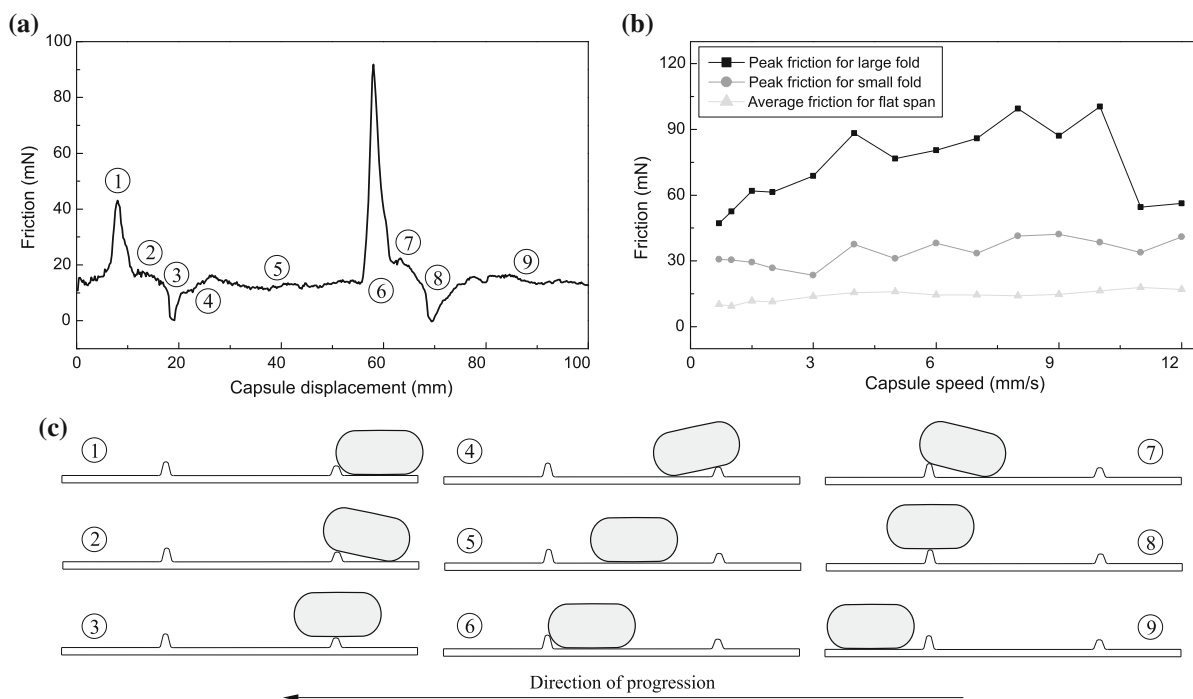
Fig. 11 a Experimental time history of the measured friction for Case 2 when the capsule was pulled at a constant speed of 8 mm/s. **b** Peak frictions (black squares) when the capsule passed the large circular fold, peak frictions (grey circles) when the capsule passed the small circular fold, and average frictions (grey triangles) when the capsule moved on the flat section of the intestine. **c** Graphic illustration of the capsule for an experimental trial showing different stages of progression
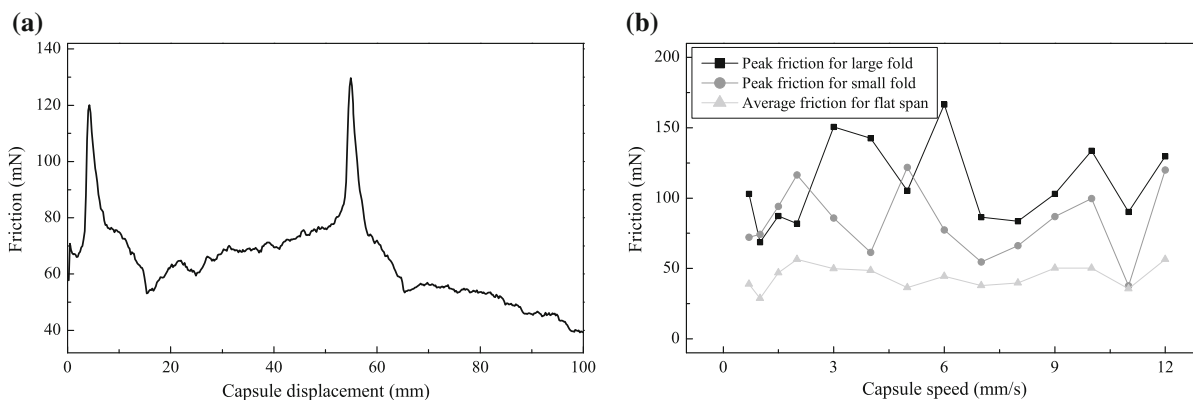

Fig. 12 a Experimental time history of the measured friction for Case 3 when the capsule was pulled at a constant speed of 12 mm/s. **b** Peak frictions (black squares) when the capsule passed the large circular fold, peak frictions (grey circles) when the capsule passed the small circular fold, and average frictions (grey triangles) when the capsule moved on the flat section of the intestine

for each test when the capsule moved along the longitudinal direction. It was impossible to keep the experimental conditions exactly the same for each test, so

more fluctuant frictions were recorded. Another observation for Case 3 is that the peak frictions for large and small circular folds are close, while for Case 2, such a
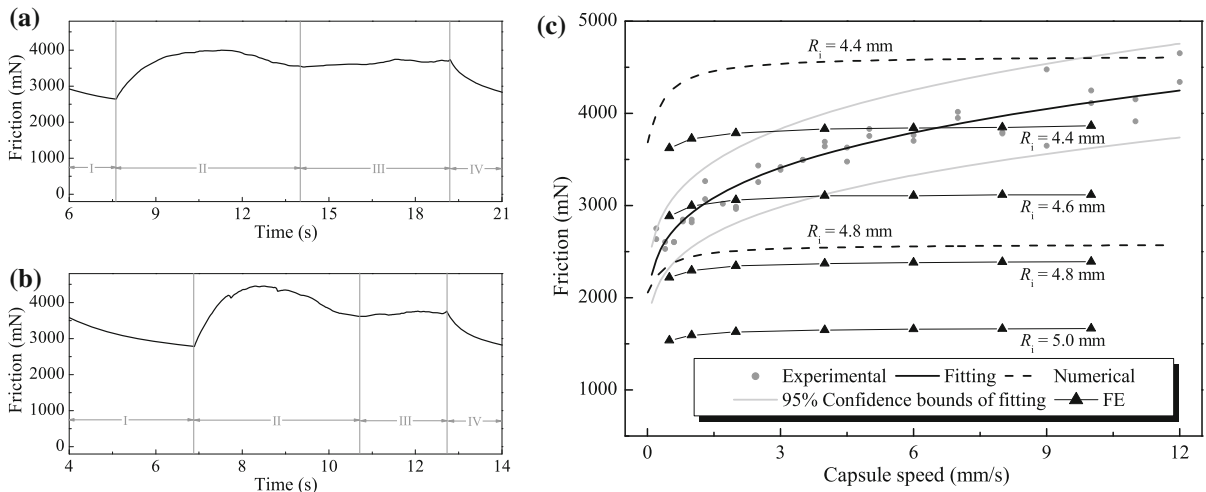
Fig. 13 Experimental time histories of Case 4 for which the capsule was pulled in a contractive small intestine at the constant progression speeds of **a** 4 mm/s and **b** 8 mm/s. Phase I: the capsule was moved to an arbitrary initial position; Phase II: the DC stepper motor pulled the capsule moving forward, and the intestine was observed moving together with the capsule, so the data were considered as transient; Phase III: the data were considered as steady and used to calculate the average friction on the capsule as no obvious movement of the intestine was observed; Phase IV: the DC stepper motor stopped pulling the capsule. **c** Average friction as a function of capsule's speed, where black dots represent average frictions, black solid line denotes the fitting of the averaged frictions, its 95% confidence bounds are depicted by grey lines, black dash lines represent the friction prediction by using Eq. (16) for the intestinal radius of $R_i = 4.4$ and 4.8 mm, and black triangles denote FE results

difference is much more obvious. So we can conclude that the dimension of the circular fold does not make significant difference on capsule's friction force when the capsule moves in a naturally collapsed small intestine. For the experimental measurements for the large fold in Fig. 12b, the maximum peak value is 170 mN, which will be used in Sect. 5 to investigate the force magnification phenomenon.

4.4 Case 4: moving in a contractive intestine

In Case 4, the capsule was pulled in a contractive intestine whose inner diameter was smaller than capsule's external diameter, so the capsule was surrounded by the intestine causing a large friction force due to the hoop stress. Figure 13a, b presents two typical time histories of the measured friction for Case 4 when the capsule was pulled at the speeds of 4 mm/s and 8 mm/s, respectively. For each time history, measurement was considered in four phases. In Phase I, the capsule was moved to an arbitrary initial position, and the measured friction decayed due to the viscoelastic property of the intestine. Similar decay trends of intestinal hoop pres-

sure were observed in our earlier study [34], where the viscoelastic property of the intestine was studied. In Phase II, the DC stepper motor pulled the capsule moving forward. As the external diameter of the capsule (11 mm) was larger than the inner diameter of the intestine (about 9 mm), the intestine was observed moving together with the capsule in this phase, so the data in Phase II were considered as transient. In Phase III, the data were used to calculate the average friction on the capsule as no obvious movement of the intestine was observed. In Phase IV, the DC stepper motor stopped pulling the capsule, and the measured friction decayed again due to the viscoelasticity of the intestine. According to the measurement in Fig. 13a, b, the average frictions in Phase III were 3641.87 mN for the capsule moving at 4 mm/s and 3973.08 mN for the capsule moving at 8 mm/s, respectively.

For Case 4, 42 experimental tests were carried out at different capsule speeds, and numerical and experimental results are compared in Fig. 13c, where black dots represent the average frictions over the time spans of Phase III, black solid line denotes the fitting of the average frictions, grey lines represent the 95% confidence bounds of the fitting, and black dash lines are
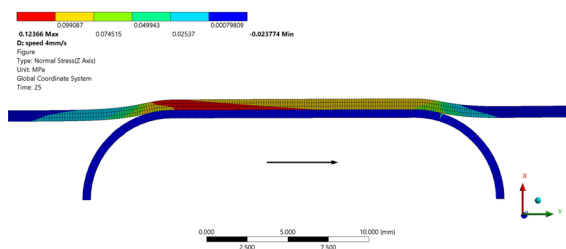
Fig. 14 Hoop stress distribution for Case 4. The capsule moved at 4 mm/s in a circumferentially contractive intestine with the radius of 5.0 mm, and the largest stress distribution was located close to the tail of the capsule

numerical predictions by using Eq. (16) for the intestinal radius of $R_i = 4.4$ mm and $R_i = 4.8$ mm. Based on the experimental results, the fitted friction–velocity relationship can be represented as

$$F_{c4e} = 1539V_c^{0.25} + 1383, \tag{18}$$

where the fitted results show a high accordance with the experimental data with the r-squared fitting goodness at 0.9073, and all the experimental data are within the 95% confidence bounds. As can be seen from Fig. 13c, numerical prediction by using Eq. (16) is not that accurate as the fitted results by using Eq. (18), but still gives some degree of fitness. One possible reason is that the intestinal friction coefficient varies as capsule's speed increases. This inference can be confirmed from Fig. 13c, where the maximum and the minimum frictions were 4500 mN measured at the progression speed of 12 mm/s and 2500 mN recorded at the progression speed of 0.4 mm/s, respectively. These maximum and minimum frictions will be used in Sect. 5 to study the force magnification phenomenon. In addition, the friction prediction for $R_i = 4.8$ mm is much smaller than the one for $R_i = 4.4$ mm, so the hoop-induced friction is very sensitive to the radial deformation of the synthetic small intestine. This can be confirmed by the FE results presented in Fig. 13c, where the radius of the small intestine varied from 5 mm to 4.4 mm, and the friction acting on the capsule increased from about 1.5 N to 3.8 N.

Figure 14 presents the hoop stress distribution when the capsule moved at 4 mm/s in a circumferentially contractive intestine with the radius of 5.0 mm. As can be seen from the figure, the largest stress distribution with an average contact pressure of 10.795 kPa was located close to the tail of the capsule, which could be

due to the stress relaxation of the synthetic material of the small intestine used in our experiments.

5 Capsule's dynamics and force magnification

For the vibro-impact capsule shown in Fig. 1b, although the excitation force on the inner mass is small, the interaction force between the inner mass and the capsule shell could reach its maximum when impact occurs, so exceeding the intestinal friction and propelling the capsule forward or backward. This vibro-impact mechanism performs as a force magnifier which can enhance capsule's progression. In this section, we will optimise this propulsive force for the capsule through mathematical modelling and numerical analysis of the millimetre-scale prototype.

5.1 Prototyping the millimetre-scale vibro-impact mechanism

As shown in Fig. 15, a millimetre-scale vibro-impact mechanism was designed, manufactured, and integrated inside a capsule shell for testing. A permanent magnet was used as the inner mass which was excited by an external magnetic field, and its motion was constrained by a linear bearing mounted inside the capsule. A helical spring was fixed to the linear bearing at one end and fixed to the inner mass at the other end. The constraint on the capsule was engineered by using a 3D-printed crossed structure to provide elasticity for the impact while keeping the total weight of the capsule at the minimum. It should be noted that the present work will focus on the optimisation of the magnification through numerical analysis of the mathematical model of the prototype. Optimisation of the geometric dimension of the constraint could also enhance the magnification, but it will be studied in another publication in due course.

5.2 Mathematical model of the prototype

According to Figs. 1b and 15a, M_m is the mass of the magnet, and M_c is the total mass of the rigid capsule consisting of the shell, the bearing, and the constraint. k and k_1 represent the stiffness of the helical spring
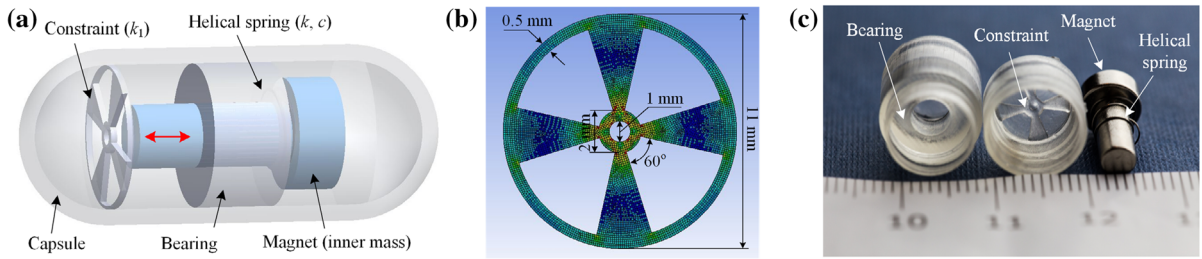
Fig. 15 (Colour online) **a** Conceptual design of the vibro-impact capsule system. A permanent magnet was used as an inner mass excited by an external magnetic field. The bearing which held the magnet, the constraint that provided impacts for the mag-net, and the capsule were all 3D-printed as a whole. A helical spring was fixed between the bearing and the magnet to provide restoring force for the magnet. **b** Dimension of the constraint. **c** Photograph of the disassembled prototype

and the constraint, respectively. Here, only the damping of the helical spring c is considered, and G_1 represents the gap between the magnet and the constraint. X_c and V_c represent the displacement and the velocity of the capsule, and X_m and V_m represent the displacement and the velocity of the magnet, respectively. When the relative displacement $X_m - X_c$ is greater than or equal to the gap G_1, the magnet will impact with the constraint. Such a collision will result in a large impact force acting on the capsule, so propel the capsule moving forward. The external excitation, F_e, is a harmonic signal written as $F_e(t) = P_d \cos(2\pi f t)$, where t is the time, P_d and f are the amplitude and the frequency of the excitation, respectively. Therefore, the governing equations of the prototype are written as

$$\begin{cases} M_m \ddot{X}_m = F_e - F_i, \\ M_c \ddot{X}_c = F_f + F_i, \end{cases} \tag{19}$$

where F_f is the intestinal friction on the capsule and F_i represents the interaction force between the capsule and the magnet written as

$$F_i = \begin{cases} k X_r + c V_r, & X_r < G_1, \\ k X_r + c V_r + k_1(X_r - G_1), & X_r \geq G_1, \end{cases} \tag{20}$$

where $X_r = X_m - X_c$ and $V_r = V_m - V_c$ represent the relative displacement and velocity between the inner mass and the capsule, respectively.

In this work, experimentally identified friction models (17) and (18) will be compared with Coulomb friction model (1), so the intestinal friction can be written as

Table 2 Identified parameters of the millimetre-scale capsule prototype

Parameter	Unit	Value
M_m	g	1.8
M_c	g	1.67
G_1	mm	1.6
k	kN/m	0.062
k_1	kN/m	27.9
c	Ns/m	0.0156

$$\begin{cases} F_f \in [-P_f, \ P_f], & V_c = 0, \\ F_f = -\mathrm{sign}(V_c) P_f, & V_c \neq 0, \end{cases} \tag{21}$$

where $P_f = F_{c1}$ for Coulomb friction,

$$\begin{cases} F_f \in [-0.0025, \ 0.0025], & V_c = 0, \\ F_f = -\mathrm{sign}(V_c) F_{c1e}, & V_c \neq 0, \end{cases} \tag{22}$$

for Case 1, and

$$\begin{cases} F_f \in [-1.3830, \ 1.3830], & V_c = 0, \\ F_f = -\mathrm{sign}(V_c) F_{c4e}, & V_c \neq 0, \end{cases} \tag{23}$$

for Case 4.

The identified physical parameters of the prototype are given in Table 2. The stiffness and damping coefficients of the helical spring were identified through free vibration test. It is worth noting that due to the dimension of the constraint, it was difficult to attach any sensor to measure the magnification force when the magnet impacts the constraint, particularly when the capsule was moving. So a FE model of the constraint was built as shown in Fig. 15b to verify the effectiveness
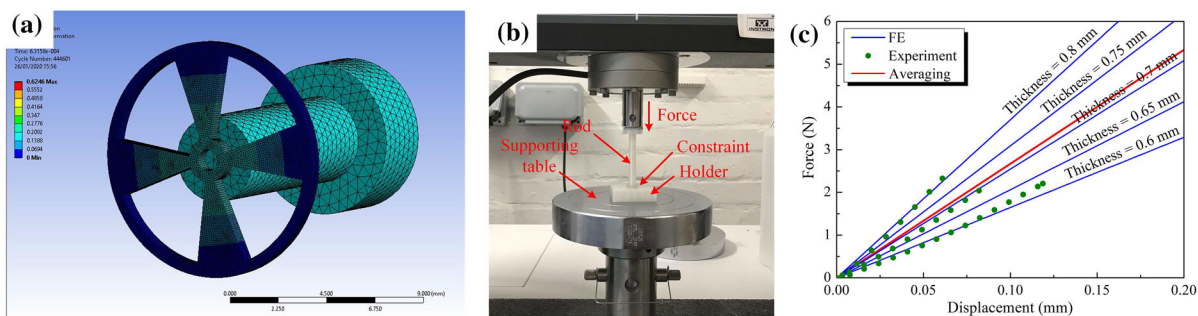
Fig. 16 (Colour online) **a** FE model, **b** experimental set-up, and **c** force–deflection curves for static testing of the constraint

of the magnification and the accuracy of the numerical analyses carried out in the next subsection.

Figure 16 presents the static testing of the constraint through FE modelling and experiment. In Fig. 16a, a FE model of static testing was developed in ANSYS WORKBENCH by using the static structural module, where a magnet applied continuous force on a fixed constraint. In Fig. 16b, experimental set-up of the static testing is shown, where the constraint was secured on a holder fixed onto a supporting table, and a continuous force acting on the constraint was applied from the Instron machine through a rod with the same diameter of the magnet. FE (blue lines) and experimental results (green dots) of static testing are presented in Fig. 16c, where three 3D-printed constraints with the same targeted thickness 0.6 mm were tested. However, due to the inaccuracy of 3D printing, the thicknesses of the constraints were slightly different leading to three different values of stiffness. In FE simulation, the constraints with different thicknesses were also simulated. It was found that they were reasonably consistent with experimental testing, and the experimental average stiffness was close to the FE model with the thickness of 0.7 mm. Finally, providing that the constraint performed linear elastic deformation, the experimental average stiffness $k_1 = 27.9$ kN/m (marked by red line) was used in the numerical simulation carried out in the next subsection.

5.3 Influence of friction models on capsule's dynamics

This subsection compares the dynamics of the prototype under Coulomb friction (21) and the friction models (22) and (23) identified experimentally in Cases

1 and 4 to demonstrate the effectiveness of Coulomb friction on predicting the dynamics of the prototype. Numerical simulations were carried out in the range of the frequency of external excitation $f \in [1, 40]$ Hz which was an adjustable frequency range in experiment. The results were presented on the bifurcation diagrams where the relative velocity V_r^*, which is a projection of the Poincaré map on the V_m-V_c axis, was plotted as a function of excitation frequency. To monitor the progression of the prototype, the average progression of the capsule per period of excitation was plotted as a function of excitation frequency.

Figure 17 presents the bifurcation diagram and the average velocity of the prototype with Coulomb friction $P_f = 7.8$ mN and the friction model (22) identified experimentally in Case 1. It can be seen from the figure that the dynamics of the prototype are similar for both friction models. As the frequency of excitation increased, the prototype experienced the transition from a nonimpacting to an impacting response. It was recorded that the first grazing was encountered at $f = 21.9$ Hz, and the prototype started to move from oscillating in place to backward progression. Then, the capsule experienced a short period of chaotic motion due to the second grazing event. A zoom-up of the chaotic range was displayed in an additional window showing two small ranges of chaos connected by a short period-4 response and finally terminated by a period-1 response with two impacts per period of excitation via a reverse period-doubling cascade. As the frequency of excitation increased further, the prototype bifurcated from the period-1 response with two impacts per period of excitation to a period-1 response with one impact per period of excitation at about $f = 28.66$ Hz. Thereafter, the impact became effective, and the prototype started to move forward from about $f = 31.76$ Hz.
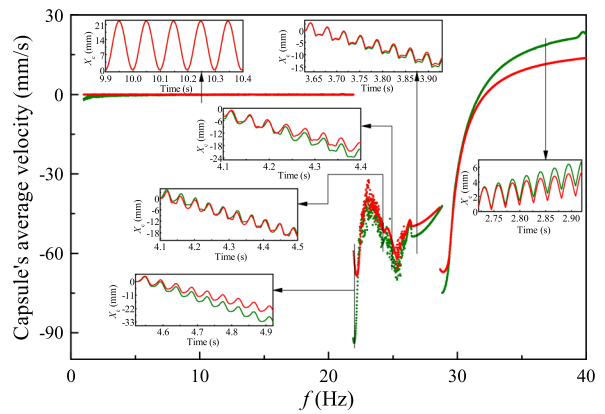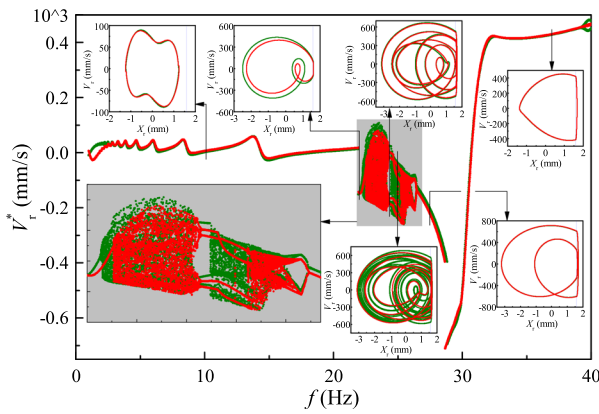
Fig. 17 (Colour online) **a** Bifurcation diagram and **b** average progression velocity of the prototype model (19) with Coulomb friction (21), $P_f = 7.8$ mN (green dots), and the friction model (22), $P_f = F_{c1e}$ (red dots), for Case 1 calculated by varying the frequency of external excitation, $P_d = 150$ mN, and using the parameters given in Table 2. Internal windows demonstrate the trajectories on the phase plane (X_r, V_r) and the time histories of capsule's displacements obtained for $f = 10.1$, 22.1, 24.4, 24.9, 27.6, and 36.8 Hz using Coulomb friction (21) (green lines) and the friction model (22) (red lines)
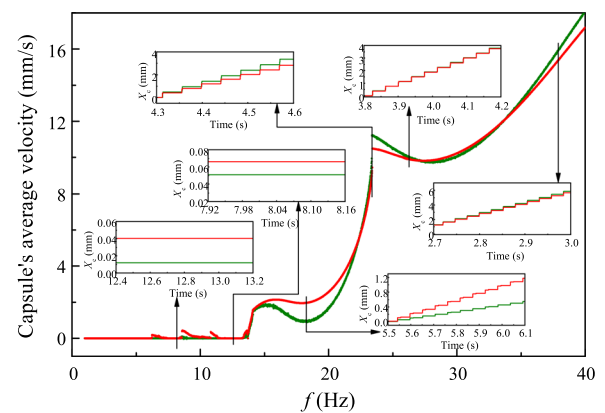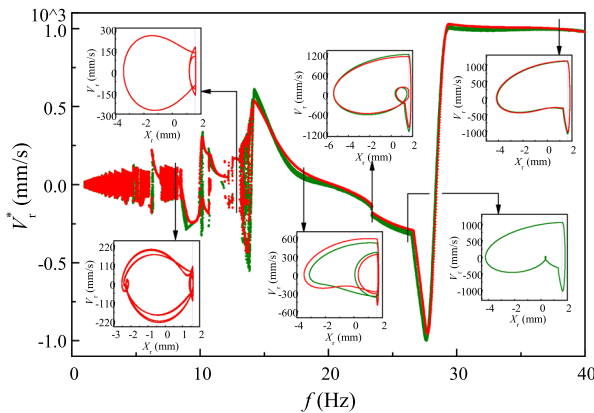

Fig. 18 (Colour online) **a** Bifurcation diagram and **b** average progression velocity of the prototype model (19) with Coulomb friction (21), $P_f = 2.5$ N (green dots), which is the minimal friction identified in experiment, and the friction model (23), $P_f = F_{c4e}$ mN (red dots), for Case 4 calculated by varying the frequency of external excitation, $P_d = 150$ mN, and using the parameters given in Table 2. Internal windows demonstrate the trajectories on the phase plane (X_r, V_r) and the time histories of capsule's displacements obtained for $f = 8.1$, 12.7, 18.2, 23.4, 26.4, and 37.9 Hz

A comparison of bifurcation diagrams and average progressions of the prototype with Coulomb friction $P_f = 2.5$ N and the friction model (23) identified experimentally in Case 4 is presented in Fig. 18, where the frequency of external excitation was varied as a branching parameter, and $P_f = 2.5$ N is the minimal friction identified experimentally in Case 4. It can be observed that the prototype had a similar dynamics with both friction models, which also revealed a similar transition as Case 1 from a nonimpacting to an impacting response when the frequency of excita-

tion was increased. The prototype had chaotic response (with a number of small windows of period-1 motion) and no significant forward progression until $f = 13.32$ Hz at where chaotic response bifurcated into a period-1 response with two impacts per period of excitation. As the excitation frequency increased, the period-1 response with two impacts evolved into a period-1 response with one impact per period of excitation at $f = 23.4$ Hz. Thereafter, the impact became more efficient, and the average progression of the prototype was faster.

The studies above suggest that the dynamics of the prototype was not influenced significantly by the friction models but the threshold of the friction, e.g. $P_f = 7.8$ mN for Case 1 and $P_f = 2.5$ N for Case 4. It also reveals that the period-1 response with one impact per period of excitation is the most efficient response for forward progression of the prototype when the frequency of external excitation is about $f > 35$ Hz. The threshold of the friction is also essential to forward and backward progression since when the friction is too large as Case 4, no backward motion can be observed.

5.4 Propulsive force magnification

To evaluate the magnification efficiency of the vibro-impact mechanism, the magnification factor is introduced as

$$A_f = \frac{\max(|F_i|)}{P_d}. \tag{24}$$

The magnification factors of the vibro-impact mechanism for various excitation frequencies and amplitudes under different intestinal frictions calculated by using Eqs. (19)–(23) are shown in Fig. 19. It is clearly seen from the figures that the frequency of the excitation affected the magnification factor, and better magnification can be obtained in the frequency range $f \in (28, 33)$ Hz. The intestinal frictions used in Fig. 19, $P_f = 0.007$ N, $P_f = 0.17$ N, 2.5 N, and 4.5 N, were the minimum friction measured in Case 1, the maximum experimental friction measured in Case 3, the minimum and maximum experimental frictions measured in Case 4, respectively. In addition, $P_f = 10$ N and $+\infty$ N were calculated to simulate the extreme cases when the capsule was stuck. As the intestinal friction increased, the maximum magnification factor increased, so the magnification effect was more remarkable for larger intestinal friction. Furthermore, it can be observed that the magnification with the friction model (22) identified experimentally in Case 1 is very similar to the ones with Coulomb frictions, $P_f = 0.007$ N, $P_f = 0.17$ N, and $P_f = +\infty$ N. The magnification with the friction model (23) identified experimentally in Case 4 is similar to the ones with Coulomb frictions, $P_f = 2.5$ N, $P_f = 4.5$ N, and $P_f = 10$ N. This consistency also confirms that Coulomb friction model (21) can be used competently to predict the dynamics of the prototype under different capsule–intestine contact conditions.

6 Conclusions

This paper studied a millimetre-scale vibro-impact capsule system for small bowel endoscopy with a specific focus on experimental and numerical investigation to predict the intestinal friction acting on the capsule by considering various capsule–intestine contact conditions. Experimental and numerical results obtained in this study can be used to guide the design and prototyping of the next generation of controllable capsule endoscope.

To measure the intestinal friction, an experimental rig was designed and self-assembled, and four capsule–intestine contact conditions were tested for a wide range of capsule's progression speeds. For Case 1, the capsule moved on a flat-open synthetic small intestine, and the measured friction is small increasing from 7 mN to 23 mN as capsule's progression speed was increased from 0.2 mm/s to 12 mm/s. Numerical prediction by using the Coulomb friction model was about 7.8 mN which has a large discrepancy from the experimental measurement. So, a fitted friction–speed relationship based on experimental measurement was proposed to describe the friction when the capsule moves on a flat-open intestine.

For Case 2, the capsule moved on an open intestine which was fixed to an arc-shape holder with a small and a large circular fold. Experimental results show that the intestinal friction jumps to a peak value when the capsule crosses over the fold, and then decreases to a trough value when capsule's gravity centre passes the fold. After the entire capsule passes the fold, it moves on a smooth section of the intestine, hence the friction is close to its counterpart recorded in Case 1. Experimental observation also indicates that the friction peaks (up to 100 mN) when the capsule passes the large fold are about two or three times larger than the ones when the capsule passes the small fold.

For Case 3, a complete synthetic small intestine was used with its bottom half fixed to the arc-shape holder and its top half naturally collapsing on the capsule due to gravity. Friction–displacement curve indicates a similar trend as Case 2, but larger frictions (up to 170 mN) were recorded.
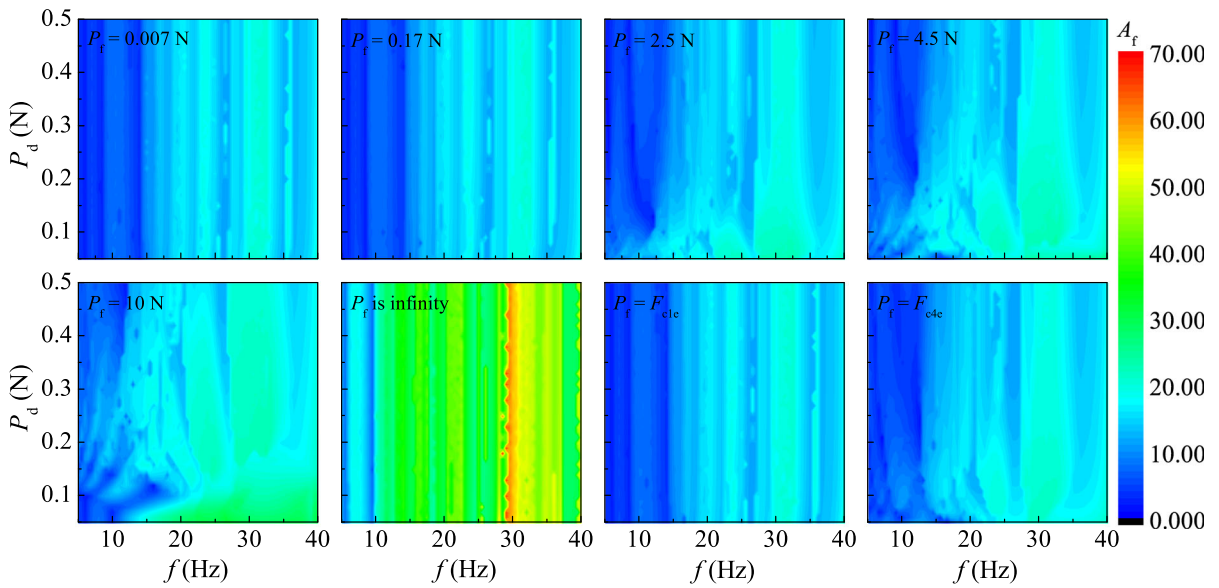
Fig. 19 (Colour online) Magnification factors calculated for $P_f = 0.007$ N, $P_f = 0.17$ N, $P_f = 2.5$ N, $P_f = 4.5$ N, $P_f = 10$ N, $P_f = +\infty$ N, $P_f = F_{c1e}$, and $P_f = F_{c4e}$, under $P_d \in [0.01, 0.5]$ N and $f \in [5, 40]$ Hz, with the other parameters obtained from Table 2

For Case 4, both experimental and numerical studies were conducted to obtain the friction acting on the capsule when the capsule moved in a contractive intestine whose inner diameter was smaller than capsule's external diameter. In this case, the intestine surrounded the capsule tightly, hence the intestinal hoop stress introduced a huge friction on the capsule, which were between 2.5 N and 4.5 N based on different capsule's progression speeds according to our experiments. Meanwhile, the discrepancy between numerical predictions and experimental results reveals that the friction coefficient is a function of capsule's progression speed, and the hoop-induced friction is very sensitive to the radius of the intestine, which could vary in a wide range during the passage in the small bowel.

To verify the proposed vibro-impact propelling mechanism, a mathematical model of the capsule prototype was developed, and a force magnification factor was introduced. When the magnet collides with the constraint, the interaction force between the magnet and the capsule increases to a peak value, which could be many times larger than its excitation force and is sufficient to overcome the measured intestinal frictions in experiments. Since direct measurement of the magnification force on the prototype was difficult in experiment, a FE model of the constraint was developed to

compare with the experimental static testing by using an Instron machine. The consistency between FE and experimental results indicates that the average stiffness of the constraint identified through experiment can be used to predict the dynamics of the prototype providing that the constraint performs linear elastic deformation.

Numerical studies indicate that friction models do not have significant influence on the dynamics of the prototype but the threshold of Coulomb friction. The period-1 response with one impact per period of excitation is the most efficient response of the prototype for forward progression. Parametric investigation also suggests that the magnification factor could be up to 70 for the excitation frequency operated between 28 Hz and 33 Hz, and the larger the intestinal friction is, the more efficient the magnification is.

Future work includes parametric optimisation, experimental verification, and *in vitro* test of the millimetre-scale prototype.

Compliance with ethical standards

Conflict of interest The authors declare that they have no conflict of interest concerning the publication of this manuscript.

References

1. Nakamura, T., Terano, A.: Capsule endoscopy: past, present, and future. J. Gastroenterol. **43**, 93–99 (2008)
2. Valdastri, P., Simi, M., Webster III, R.J.: Advanced technologies for gastrointestinal endoscopy. Annu. Rev. Biomed. Eng. **14**, 397–429 (2012)
3. Gerson, L., Fidler, J.L., Cave, D.R., Leighton, J.A.: ACG clinical guideline: diagnosis and management of small bowel bleeding. Am. J. Gastroenterol. **110**(9), 1265–1287 (2015)
4. Sidhu, R., Sanders, D.S., Morris, A.J., McAlindon, M.E.: Guidelines on small bowel enteroscopy and capsule endoscopy in adults. Gut **57**(1), 125–136 (2008)
5. Li, F., Gurudu, S.R., De Petris, G., Sharma, V.K., Shiff, A.D., Heigh, R.I., Fleischer, D.E., Post, J., Erickson, P., Leighton, J.A.: Retention of the capsule endoscope: a single-center experience of 1000 capsule endoscopy procedures. Gastrointest. Endosc. **68**(1), 174–180 (2008)
6. Sendoh, M., Ishiyama, K., Arai, K.I.: Fabrication of magnetic actuator for use in a capsule endoscope. IEEE Trans. Magn. **39**(5), 3232–3234 (2003)
7. Kim, B., Park, S., Park, J.O.: Microrobots for a capsule endoscope. In: IEEE/ASME International Conference on Advanced Intelligent Mechatronics, pp. 729–734. IEEE (2009)
8. Quirini, M., Menciassi, A., Scapellato, S., Stefanini, C., Dario, P.: Design and fabrication of a motor legged capsule for the active exploration of the gastrointestinal tract. IEEE/ASME Trans. Mech. **13**(2), 169–179 (2008)
9. Park, H., Park, S., Yoon, E., Kim, B., Park, J., Park, S.: Paddling based microrobot for capsule endoscopes. IEEE Int. Conf. Robot. Autom. **1**, 3377–3382 (2007)
10. Liu, Y., Guo, B., Prasad, S.: Resonance enhanced self-propelled capsule endoscopy for small bowel examination. Gut **68**, A31 (2019)
11. Liu, L., Towfighian, S., Hila, A.: A review of locomotion systems for capsule endoscopy. IEEE Rev. Biomed. Eng. **8**, 138–151 (2015a)
12. Chernous'ko, F.L.: The optimum rectilinear motion of a two-mass system. J. Appl. Math. Mech. **66**(1), 1–7 (2002)
13. Liu, Y., Wiercigroch, M., Pavlovskaia, E., Yu, H.: Modelling of a vibro-impact capsule system. Int. J. Mech. Sci. **66**, 2–11 (2013a)
14. Guo, B., Liu, Y., Birler, R., Prasad, S.: Self-propelled capsule endoscopy for small-bowel examination: proof-of-concept and model verification. Int. J. Mech. Sci. **174**, 105506 (2020)
15. Liu, Y., Pavlovskaia, E., Wiercigroch, M., Peng, Z.: Forward and backward motion control of a vibro-impact capsule system. Int. J. Non-Linear Mech. **70**, 30–46 (2015b)
16. Glass, P., Cheung, E., Sitti, M.: A legged anchoring mechanism for capsule endoscopes using micropatterned adhesives. IEEE T. Biomed. Eng. **55**(12), 2759–2767 (2008)
17. Liu, Y., Pavlovskaia, E., Hendry, D., Wiercigroch, M.: Vibro-impact responses of capsule system with various friction models. Int. J. Mech. Sci. **72**, 39–54 (2013b)
18. Liu, Y., Pavlovskaia, E., Wiercigroch, M.: Experimental verification of the vibro-impact capsule model. Nonlinear Dyn. **83**, 1029–1041 (2016)
19. Liu, Y., Páez Chávez, J., Guo, B., Birler, R.: Bifurcation analysis of a vibro-impact experimental rig with two-sided constraint. Meccanica (2020). https://doi.org/10.1007/s11012-020-01168-4
20. Kim, J.S., Sung, I.H., Kim, Y.T., Kwon, E.Y., Kim, D.E., Jang, Y.H.: Experimental investigation of frictional and viscoelastic properties of intestine for microendoscope application. Tribol. Lett. **22**(2), 143–149 (2006)
21. Wang, X., Meng, M.: An experimental study of resistant properties of the small intestine for an active capsule endoscope. Proc. Inst. Mech. Eng. H. **224**(1), 107–118 (2010)
22. Zhang, C., Liu, H., Tan, R., Li, H.: Modeling of velocity-dependent frictional resistance of a capsule robot inside an intestine. Tribol. Lett. **47**(2), 295–301 (2012)
23. Accoto, D., Stefanini, C., Phee, L., Arena, A., Pernorio, G., Menciassi, A., Carrozza, M.C., Dario, P.: Measurements of the frictional properties of the gastrointestinal tract. In: World Tribology Congress, pp. 728–731 (2001)
24. Zhang, H., Yan, Y., Gu, Z., Wang, Y., Sun, T.: Friction enhancement between microscopically patterned polydimethylsiloxane and rabbit small intestinal tract based on different lubrication mechanisms. ACS Biomater. Sci. Eng. **2**(6), 900–907 (2016)
25. Kim, J.S., Sung, I.H., Kim, Y.T., Kim, D.E., Jang, Y.H.: Analytical model development for the prediction of the frictional resistance of a capsule endoscope inside an intestine. Proc. Inst. Mech. Eng. H. **221**(8), 837–845 (2007)
26. Wang, Z., Ye, X., Zhou, M.: Frictional resistance model of capsule endoscope in the intestine. Tribol. Lett. **51**(3), 409–418 (2013)
27. Zhou, H., Alici, G., Than, T.D., Li, W.: Modeling and experimental investigation of rotational resistance of a spiral-type robotic capsule inside a real intestine. IEEE/ASME Trans. Mech. **18**(5), 1555–1562 (2013)
28. Jian, Xu, Fang, Hongbin: Improving performance: recent progress on vibration-driven locomotion systems. Nonlinear Dyn. **98**(4), 2651–2669 (2019)
29. Fang, Hongbin, Wang, K.W.: Piezoelectric vibration-driven locomotion systems-exploiting resonance and bistable dynamics. J. Sound Vib. **391**, 153–169 (2017)
30. Zhouwei, Du, Fang, Hongbin, Zhan, Xiong, Jian, Xu: Experiments on vibration-driven stick-slip locomotion: a sliding bifurcation perspective. Mech. Syst. Signal Pr. **105**, 261–275 (2018)

31. Guo, Bingyong, Liu, Yang: Three-dimensional map for a piecewise-linear capsule system with bidirectional drifts. Phys. D **399**, 95–107 (2019)
32. SynDaverLabs. Small Intestine. Accessed September 5, 2018. http://syndaver.com/shop/syndaver
33. Sliker, L.J., Ciuti, G., Rentschler, M.E., Menciassi, A.: Frictional resistance model for tissue-capsule endoscope sliding contact in the gastrointestinal tract. Tribol. Int. **102**, 472–484 (2016)
34. Guo, B., Liu, Y., Prasad, S.: Modelling of capsule-intestine contact for a self-propelled capsule robot via experimental and numerical investigation. Nonlinear Dyn. **55**(1), 3155–3167 (2019)
35. Gere, J.M., Goodno, B.J.: Mechanics of Materials, Brief edn. Cengage Learning, London (2012)
36. Yan, Y., Liu, Y., Manfredi, L., Prasad, S.: Modelling of a vibro-impact self-propelled capsule in the small intestine. Nonlinear Dyn. **96**(1), 123–144 (2019)
37. Medtronic. PillCam^{tm} SB 3 System. Accessed December 27, 2019. https://www.medtronic.com/